ELSEVIER

Interannual and seasonal behavior of Martian residual ice-cap albedo

S. Byrne[a,*], M.T. Zuber[a,b], G.A. Neumann[a,b]

[a]*Department of Earth, Atmospheric and Planetary Sciences, Lunar and Planetary Laboratory, University of Arizona, Tucson, AZ 85721-0092, USA*
[b]*Laboratory for Terrestrial Physics, NASA Goddard Space Flight Center, USA*

Abstract

The Mars Orbiter Laser Altimeter (MOLA), functioning as a high-resolution radiometer, has observed several appearances of the Martian residual ice caps. We examine these data to quantify both seasonal behavior and interannual differences. The northern residual cap (NRC) was found to be mostly stable with the exception of one, previously identified, region of strong variability. Interannual change in the extent of the NRC appears to be small and reversible on timescales of 1 or 2 years. The NRC has an elaborate seasonal evolution of albedo. Annuli of fine-grained CO_2 and water frost, which track the inner and outer edges of the seasonal CO_2 cap, cause large temporary brightenings. The NRC albedo is stable from just after solstice to L_s 150°, after which albedo decreases steadily. This late-summer darkening can be explained by shadowing within the rough topography of the NRC, leading to a lower limit on topographic relief of 80 cm. The southern residual cap (SRC) appears stable in extent. As has been previously discovered, its seasonal frost albedo behavior appears to be correlated with insolation. However, residual CO_2 appears not to share this characteristic; we use this behavioral difference to infer net deposition of CO_2 ice on the SRC during 1 out of 3 years. Uncharacteristically, the SRC abruptly darkens at L_s 320° in 1 Martian year (year beginning April 2002). Circumstantial evidence suggests atmospheric scattering by dust is responsible. The 2001 global dust-storm appears, either, to have had no effect on the polar cap albedos, or, resulted in slightly brighter ice deposits.
© 2007 Elsevier Ltd. All rights reserved.

Keywords: Mars; Polar; Ice; Albedo; Radiometry; Interannual

1. Introduction

The polar deposits of Mars have, for many years, been appreciated to be a record of the recent climatic history of the planet. The deposits visible at both poles are composed of quasi-domes of layered sequences (Murray et al., 1972) up to 3 km thick (Zuber et al., 1998; Smith et al., 2001a), which are now commonly interpreted as mixtures of atmospherically deposited water ice and dust (Cutts, 1973; Thomas et al., 1992; Clifford et al., 2000) although their exact composition remains unknown. Minor inclusions of CO_2 ice and clathrate are also possible but are not thought to be significant (Mellon, 1996; Nye et al., 2000). The layered deposits at both poles are incised with numerous dark lanes, which are troughs and scarps that display exposures of their layered interior.

After each (Martian) year these layered deposits are covered with approximately a meter of CO_2 ice (Leighton and Murray, 1966; Smith et al., 2001b). These seasonal ice caps disappear in the summer; however, their retreat uncovers bright residual ice caps (Fig. 1) that persist throughout the rest of the year and partially cover the underlying layered deposits. On the north polar layered deposits (NPLD) the northern residual ice cap (NRC) is composed of H_2O ice (Kieffer et al., 1976). The visible albedo of this ice is lower than what may be expected from examples of terrestrial ice, indicating that it may either be contaminated with dust or be composed of large-grains (Kieffer, 1990). Recent hyper-spectral observations (Langevin et al., 2005) have resolved this ambiguity and shown the NRC ice to be composed of large, dust-free, ice grains. The NRC thickness is unknown; however, it is thin enough to vary in lateral extent from year to year (Malin and Edgett, 2001). On the south polar layered deposits (SPLD) the southern residual ice cap (SRC) is composed of high-albedo solid CO_2 (Kieffer, 1979). It is of the order of

*Corresponding author. Tel.: +1 520 6260407; fax: +1 520 6214933.
E-mail address:* shane@lpl.arizona.edu (S. Byrne).

Nomenclature

e	eccentricity of Martian orbit (0.0934)
I_{MOLA}	radiance emitted by the surface in the MOLA band pass
J_{MOLA}	irradiance received by the surface in the MOLA band pass
L_s	solar longitude, where zero is northern spring equinox
r	bidirectional reflectance of the surface
I/F	brightness of a surface compared to a perfect diffusely reflecting surface
A_L	Lambert albedo of the surface
w	single scattering albedo
H	isotropic scattering functions (see Eq. (4))

i	solar incidence angle
g	phase angle
μ_0	cosine of the incidence angle
μ	cosine of the emission angle
P	surface scattering phase function
k	asymmetry parameter (used in P)
f	weighting between forward and backward scattering (used in P)
A_o	apparent Lambert albedo of the surface (darkened due to sub-resolved shadows)
A_t	true Lambert albedo of surface
c	ratio of shadow brightness to that of illuminated terrain
h	relief of texture on NRC (see Fig. 11)
x	length-scale of texture on NRC (see Fig. 11)

a few meters thick (Byrne and Ingersoll, 2003; Tokar et al., 2003; Prettyman et al., 2004), and has areas at its margins and in its interior where the underlying water ice of the layered deposits shows through (Titus et al., 2003; Bibring et al., 2004; Prettyman et al., 2004).

In addition to their compositional differences, the residual ice caps have distinctly different appearances when viewed at high resolution. High-resolution imagery (Thomas et al., 2000) shows that the surface of the northern residual cap has an extremely rough but homogenous texture at length scales of 10–20 m (Fig. 1E). This contrasts sharply with its bland visual appearance and smooth topography (Aharonson et al., 2001) at longer length scales and smooth appearance inferred from bistatic radar reflections at length scales of centimeters to meters (Simpson and Tyler, 1981). Thomas et al. (2000) also reported a wide range of morphologies on the SRC ranging from quasi-circular depressions to linear ridges (Fig. 1C and D). The inclined walls of these quasi-circular depressions retreat by several meters each year (Malin et al., 2001; Thomas et al., 2005), which may indicate that the SRC is in the process of disappearing. However, this sublimated CO_2 may be re-deposited on nearby flat surfaces rather than permanently lost to the atmosphere. Under current conditions, the SRC exists in a precarious position, where its stability depends critically on its ability to maintain a high albedo (Jakosky and Haberle, 1990). Monitoring of the SRC albedo is therefore a useful measure of any climatic change that may be in progress on Mars.

Similarly, the NRC plays an important role in the current climate being an important source of atmospheric water vapor. In addition, volatile deposition on the bright and cold NRC may be forming additional polar-layered deposits today. Understanding the connection of the NRC to the present climate is therefore crucial to understand the connection between the layered deposits and the previous climates which they record.

In this paper, we compare the brightness of the residual polar caps over several Martian years. We use radiometry measurements collected by the Mars Orbiter Laser Altimeter (MOLA), aboard the Mars Global Surveyor (MGS) spacecraft (Albee et al., 1998, 2001), in this effort. The 93° inclination of the MGS orbit results in convergence of orbital ground-tracks near the poles which means that complete albedo maps of both residual caps can be generated with these data spanning a short range of season and with little or no interpolation. A less welcome result of this geometry is a paucity of observations in the latitude range 87–90° at both poles.

The specifics of the instrument are discussed in the next section. At the time of writing the available record of MOLA radiometry data covers two complete and two partial Martian years. Table 1 summarizes our nomenclature convention for these various years and should facilitate comparison of this paper's results with those of others.

Continuous, multi-year, observations of the residual caps have only become possible since the arrival of the MGS spacecraft. However, earlier studies concentrating on data acquired during the Viking and Mariner 9 missions have also been undertaken. James et al. (1979, 1992) compared the appearance of the SRC in the Mariner 9 (1972) and Viking (1977) epochs and showed the earlier apparition to be much patchier in nature. Observations by James and Martin (1985) and Kieffer (1990) suggested that the NRC was variable in extent from year to year. However, a re-analysis by Bass et al. (2000) showed this to be due to seasonal, rather than inter-annual, change.

Data from years 2 and 3 from the Mars Orbiter Camera (MOC) showed definite changes in NRC extent (Malin and Edgett, 2001), indicating that interannual as well as seasonal changes were possible. In contrast, Benson and James (2005) examined the SRC extent during the years 2, 3 and 4 for interannual change but found only minor variations.
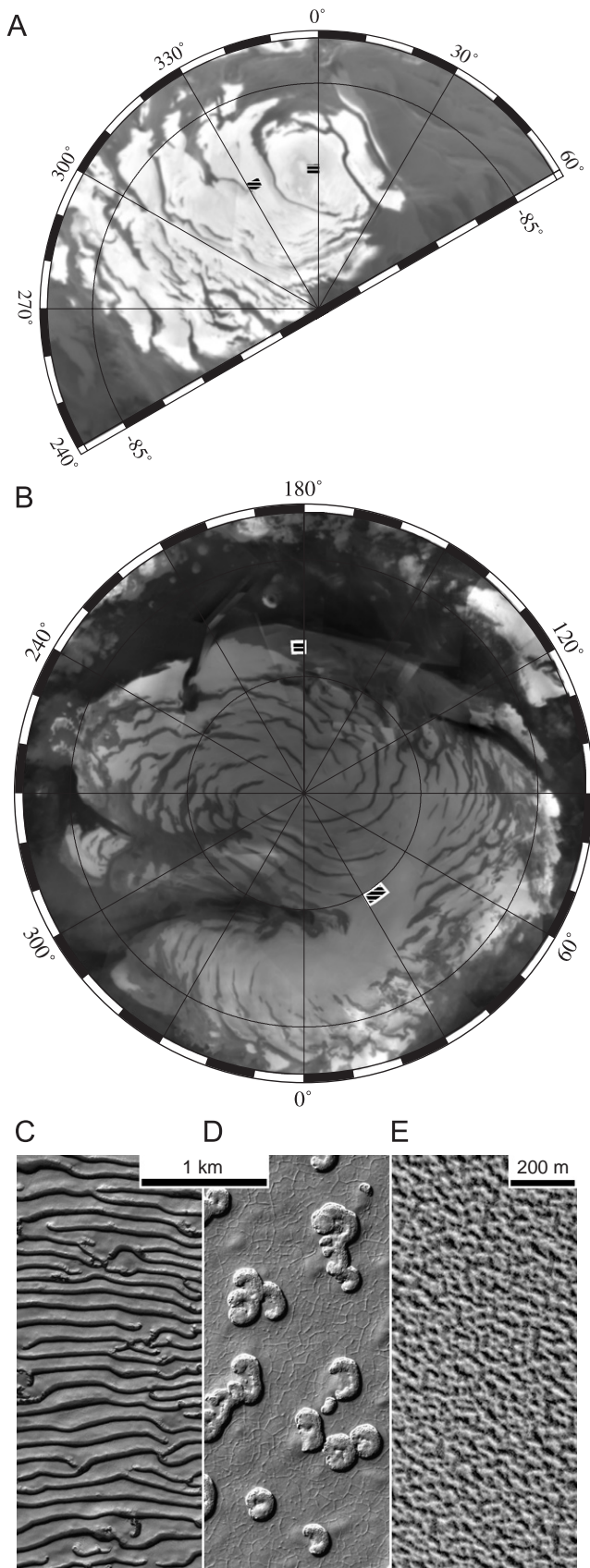
Table 1
Mars chronology conventions for this paper

Year	Terrestrial dates	Ephemeris time (Ms)	North	South
1	8/1996–7/1998	−105.638 to −46.285	No data	Aerobraking
2	7/1998–5/2000	−46.285 to 13.070	Mapping	Mapping
3	5/2000–4/2002	13.070 to 72.424	Mapping	Extended
4	4/2002–3/2004	72.424 to 131.776	Extended	Extended
5	3/2004–1/2006	131.776 to 191.132	Extended	No data

MGS and Mars Pathfinder arrive during what we term year 1; however, MGS mapping data do not become available until part-way through year 2.

Analysis of NRC brightness at the geographic north pole from MOC wide-angle data showed only minor seasonal and inter-annual differences (Benson and James, 2005) during years 2, 3 and 4. Hale et al. (2005) examined six regions of interest on the NRC in these same 3 years and found that although brightness trends are spatially variable they are generally repeatable from year to year. Analysis of NRC Thermal Emission Spectrometer (TES) albedo data (Calvin and Titus, 2004) also shows considerable variation in behavior from location to location.

Information on interannual variability can also be extracted from seasonal cap retreat rates. This is beyond the scope of this paper; good summaries have been provided from MOC data by Benson and James (2005) and TES data by Titus (2005).

Seasonal evolution of the residual caps and the seasonal frost, which covers them, have also been extensively described. The albedo of the SRC has been observed to increase in proportion to the incident insolation (Paige, 1985; James et al., 1992, 2001; Kieffer et al., 2000). Kieffer et al. (2000) showed that CO_2 grain size plays a dominant role in setting the albedo of the SRC region and other parts of the seasonal cap. Colaprete et al. (2005) showed that topographically driven atmospheric circulation controls the CO_2 frost grain size and, by extension, the cap albedo, which may explain the current non-polar location of the SRC. The seasonal evolution of NRC albedo during year 2 has been described by Kieffer and Titus (2001), who identified spatial differences in behavior.

During year 1 of the MGS mission, data were collected in the aerobraking and science-phasing parts of the mission. These data are not discussed in this paper; a thorough discussion of the year 1 behavior of the southern

Fig. 1. Polar stereographic views of the southern (A) and northern (B) residual polar caps. In this and subsequent map views, parallels and meridians are plotted every 5° and 30°, respectively. These albedo data were taken from the MOC wide angle image atlas (Caplinger and Malin, 2001). Inset views (C–E) show sample high-resolution texture from both residual caps. The SRC shows a considerable variety of surface geomorphologies both circular (D; R08/01050) and linear (C; E14/00648) in form. The NRC appears homogeneous at the scale of the MOC narrow angle observations, displaying alternating pits and mesas 10–20 m across in many locations (E; E23/01209). Illumination is from the lower right in (C) and (D), and from the upper right in (E).

polar cap is available in Kieffer et al. (2000), the northern cap was not observed by MGS during year 1. The MGS mapping mission began in year 2 at L_s 104°, early enough to observe both residual caps during this year.

In year 3, several events occurred that will influence interpretation of the interannual comparisons presented in this paper. First, the MOLA timing oscillator failed at L_s 180°, which caused the laser itself to cease firing, although the detector continued to function. A data gap of several months ensued while the instrument was tested and reprogrammed to act exclusively as a radiometer. Differences between these two operation modes are discussed in the following section. Secondly, during this no-data period, the MGS mapping mission ended and the extended mission began; the spacecraft was reoriented from nadir-pointing mode to relay-16 mode to conserve fuel. Data acquired in this latter mode have emission angles close to 18°. Finally, also during the MOLA no-data period, a planet-wide dust storm occurred, which had largely dissipated (Smith et al., 2002) by the time MOLA observations recommenced at L_s 250°. To date, this is the only global dust storm during the MGS mission (in 2001). Although the 2001 storm itself was unobserved by MOLA, its effects on the polar caps can be examined and will be discussed in later sections.

At the time of writing, MOLA radiometry data are available throughout year 4 and up to L_s 200° of year 5. Some small gaps in this coverage exist and are mostly due to solar conjunctions, along with occasional spacecraft glitches. MOLA continues to acquire data, further extending the record discussed here. The length, and near-continuous nature, of this record make it ideal for studies of temporally variable phenomena such as those related to the atmosphere or polar caps.

The following section will describe the MOLA radiometry dataset in more detail. Section 3 will present the radiometry observations. Interpretation and discussion of these observations will be presented in Section 4. Longitudes and latitudes quoted in this paper will be relative to the IAU 2000 pole vector and prime meridian (Seidelmann et al., 2002), latitudes will be in areocentric form and longitudes will increase to the east. Season will be quoted in the usual manner, i.e. areocentric longitude of the Sun (L_s).

2. MOLA radiometry dataset

The MOLA (Zuber et al., 1992) operated as an altimeter for 4 years, recording over 600 million accurate measurements of Martian topography (Smith et al., 2001a). Secondary objectives of the MOLA investigation included observations of laser pulse spreading (Neumann et al., 2003a) to characterize surface roughness and measurement of the albedo of Mars both actively (from reflected laser energy) (Neumann et al., 2003b) and passively (from reflected sunlight). In this paper we concern ourselves only with the passive radiometry.

MOLA ceased collecting altimetry measurements in mid-2001 when its timing oscillator failed. During acquisition of altimetry, MOLA also passively sensed reflected sunlight from the Martian surface at the laser wavelength (1064 ± 1.1 nm). The purpose of the observation was to provide a measure of the infrared background at the laser wavelength to enable the detection threshold setting in the MOLA receiver to be set so as to optimize the altimetry measurement (Zuber et al., 1992; Abshire et al., 2000). The passive radiometry measurements are distinct from measurements of the reflected laser energy in that they can be made without firing the laser. MOLA has continued to make these radiometry measurements since the oscillator failure. It has acquired a unique global dataset, distinguished from previous radiometric measurements by its extremely high spatial resolution and extremely narrow bandwidth.

The MOLA detector has an 800-μrad field of view and a 2.2-nm-wide spectral filter centered on 1.064 μm. In the receiver, reflected photons are amplified and pass through four parallel channels, each of which is sensitive to different degrees of spreading in the arrival time of the laser pulse (channel 1 is sensitive to the narrowest returns; channel 2 is three times wider, etc.). As channel 1 readings were saturated and therefore unusable for radiometry during much of the mapping mission this paper utilizes data from channel 2 of the MOLA instrument for all the years discussed.

During the MGS mapping mission, when altimetry measurements had priority, background photon counts were averaged over 1-s intervals to produce background flux measurements (Abshire et al., 2000). Knowledge of the observational geometry and the solar insolation on the target can be used to convert this flux to a bi-directional reflectance. The spatial scale of these measurements was approximately 300 m across the spacecraft orbital track, and 3 km along track. After MOLA ceased operating as an altimeter, the instrument was reconfigured and optimized for radiometry measurements. Noise counts are now recorded eight times a second, producing an along-track resolution of roughly 400 m. These radiometry-only measurements commenced in October of 2001 (L_s 250°, year 3) and are significantly less noisy than the measurements made during altimetry acquisition. As discussed in the introduction, the MGS spacecraft was reoriented between the acquisition of the mapping data and extended-mission data. Therefore, all mapping data presented here were acquired with an emission angle of ∼0° and all extended mission data were acquired with an emission angle of ∼18°.

The MOLA radiance measurements have been calibrated by Sun et al. (2006) using data from the TES (Christensen et al., 1992, 2001) and the wide field planetary camera on the Hubble Space Telescope (HST) (Bell et al., 1997, 1999). Indications from these calibration efforts are that the instrument response has been stable over the duration of the MGS mapping and extended missions and agrees well with pre-launch testing. After non-linear instrumental effects are removed, a single multiplicative factor of 1.4

(Sun et al., 2006) can be used on the entire dataset to bring it into agreement with the Hubble data. While the MOLA data are only empirically calibrated in an absolute sense, the high stability of the measurements makes the dataset valuable for study of temporal phenomena on Mars.

3. Observations

Measurements of radiance at the MOLA wavelength (I_{MOLA}) can be converted to a bidirectional reflectance (r) by dividing by the solar irradiance at the MOLA wavelength (J_{MOLA}). Taking the effective temperature of the solar surface to be 5778 K, J_{MOLA} at the orbit of Mars (1.5236 AU) is 272.6 mW m^{-2} nm^{-1}. This quantity varies with position in Mars' orbit and is modified by an L_s and eccentricity (0.0934 for Mars) dependent factor shown in Eq. (1):

$$J_{\mathrm{MOLA}} = 272.6 \left[\frac{1 - e^2}{1 + e \cos(L_s - 250.87^\circ)} \right]^{-2} \mathrm{mW\,m^{-2}\,nm^{-1}}. \tag{1}$$

Multiplying the bidirectional reflectance by π will yield the commonly used I over F measurement. Multiplying the bidirectional reflectance by (π/μ_0) will provide the Lambert albedo, A_{L}, where μ_0 is the cosine of the incidence angle. These relationships are summarized in Eq. (2):

$$r = \left(\frac{1}{J_{\mathrm{MOLA}}} \right) I_{\mathrm{MOLA}}, \quad \left(\frac{I}{F} \right) = \left(\frac{\pi}{J_{\mathrm{MOLA}}} \right) I_{\mathrm{MOLA}},$$
$$A_{\mathrm{L}} = \left(\frac{\pi}{\mu_0 J_{\mathrm{MOLA}}} \right) I_{\mathrm{MOLA}}. \tag{2}$$

For the purposes of interannual comparisons and seasonal behavior, we will speak in terms of Lambert albedo. In general, the range of observational geometry is sufficiently small that use of the Lambert scattering law is sufficient. Toward the end of this section, in order to constrain the scattering properties of the residual cap materials, we will examine non-Lambert behavior using the semi-analytic models of Hapke (1993). In general, we make no attempt to separate the surface and atmospherically scattered light. Atmospheric scattering is discussed in the final section as an explanation for some anomalous behavior of the SRC. We have also not attempted to change the calibration of Sun et al. (2006). Their calibration was performed over generally low albedo terrain and so may not be optimal for very high albedo values. We have also applied the correction factor, which they derived (1.4) by comparison to the HST data to the raw MOLA radiance measurements. We have found the polar cap albedos generated from MOLA data to be slightly higher than canonical values discussed by other authors. This is partly due to differences in the wavelength of observation and MOLA's narrow bandwidth. Both MOC and TES integrate visible light over a relatively wide bandwidth and so cannot be reliably compared to MOLA. James et al. (2005) used extremely well-calibrated HST

data to analyze SRC albedo from year 4 at three different seasons. A comparison with simultaneously acquired MOLA data on a typical SRC area shows that the MOLA data agrees with these measurements to within 5%. Additionally, the OMEGA instrument has acquired NRC spectra during year 5 (Langevin et al., 2005). These spectra include the MOLA wavelength. A visual comparison of simultaneous and co-located MOLA data with their Fig. 4 indicates MOLA-derived albedos to be 5–10% higher. Both of these comparisons are slightly suspect as the observational geometry is different in each case. However, as we are mostly concerned with albedo changes over seasonal and annual timescales, the absolute calibration is not as important as the instrument stability (which appears excellent).

Although the northern and southern residual caps are generally only visible for a fraction of the year, the convergence of orbital tracks at the poles means that close to complete coverage can be achieved during each appearance. The larger size of the northern residual cap is offset by its longer exposure duration. Fig. 2 shows the residual caps as seen by MOLA during the years for which they were observed (see Table 1). This figure includes data collected over the entire period where the residual caps were exposed (L_s 110–170° and L_s 320–340° for the NRC and SRC, respectively) and so masks considerable seasonal variation, which will be discussed in more detail below.

In general, the outline of the NRC does not change significantly from year to year. The bright material at the cap edge in the region of 180°E shows the most variability, being much darker in year 2 than subsequent years. This behavior was previously reported by Malin and Edgett (2001) in their review of the MOC mapping data. A similar darkening takes place at the westernmost point of the lobe of material south of Chasma Boreale (82°N, 330°E) during year 3. This has partially recovered during year 4 and by year 5 is indistinguishable from its pre-darkening albedo in year 2. The picture which emerges is one of a mostly stable NRC which experiences small patches of darkening that are quickly reversible on the timescale of Martian years.

In the case of the SRC, there was no noticeable change in the extent of the cap in the 3 years observed. In terms of the cap interior brightness, there is little difference between years 2 and 3; however, year 4 had a much lower albedo. Although this darkening was mostly constant throughout the whole of the SRC there was one region, at 87°S and 330°E, which appears to have darkened more than the surrounding areas.

Fig. 3A and C shows the differences in residual cap Lambert albedo between the first and last available years for both poles. The region 110–200°E at the edge of the NRC stands out clearly as having the largest albedo change of 0.1 (~20%). Other increases in albedo are visible at 84°N, 30°E and 81°N, 290°E, but these are small, in both degree and extent, by comparison. In the SRC, the cap as a whole has darkened by 0.1–0.15 (15–20%) due to the anomalous behavior at the end of year 4 mentioned above.
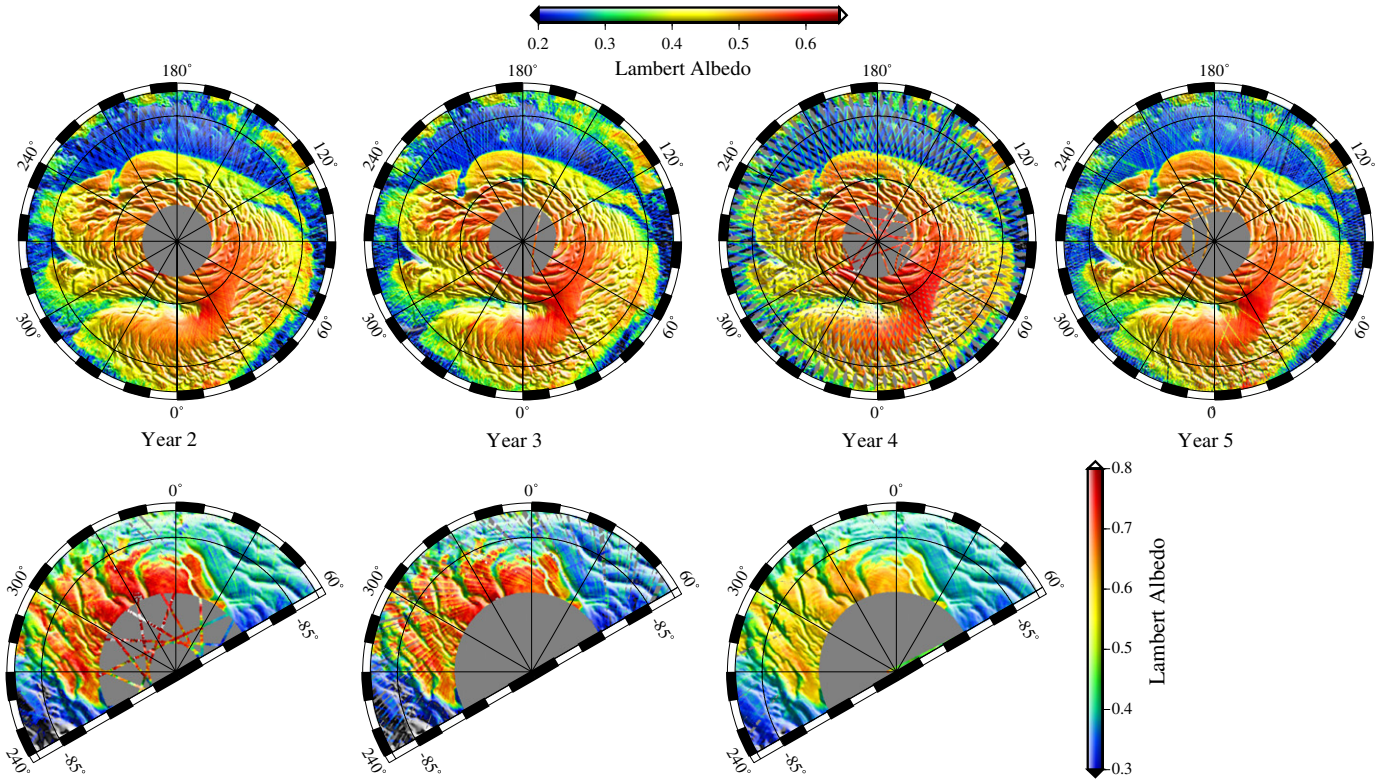
Fig. 2. Map views of Lambert albedo over the northern and southern residual caps for each appearance available. Northern data extend from L_s 110 to 170°; southern data extend from L_s 330 to 350°. Note separate albedo scales for each pole.
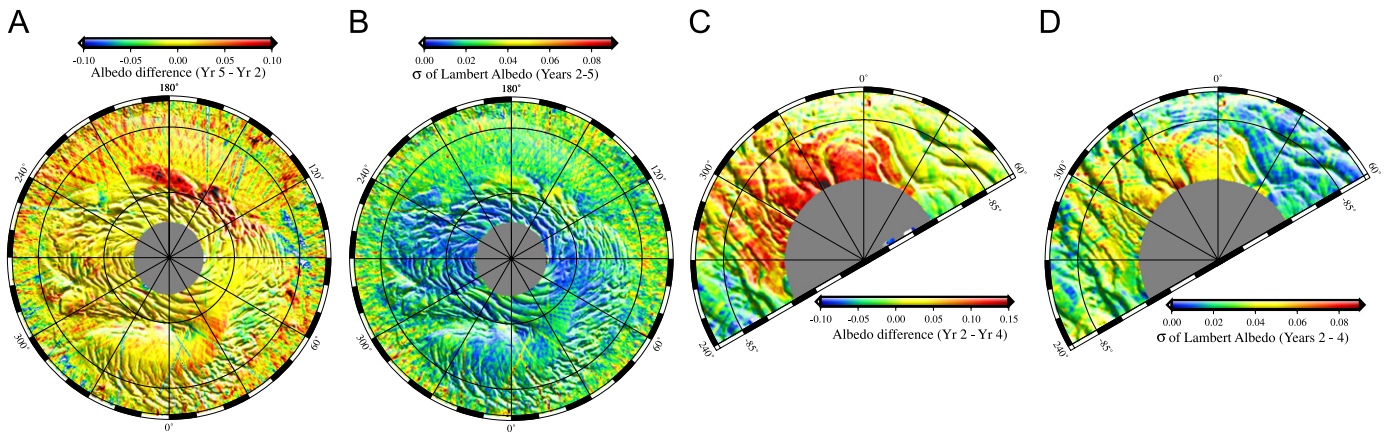

Fig. 3. Interannual changes in residual cap Lambert albedo. (A) Difference in Lambert albedo of the NRC between years 5 and 2. The majority of the cap is unchanged except for an area close to 84°N, 180°E. (B) Standard deviation of the 4 NRC albedo measurements at each point, strong variation is seen in the same region discussed in (A), much milder variation is seen east and south of Chasma Boreale. (C) Similar to (A) for the SRC. The residual cap darkened as a whole during year 4, the region around 87°S, 335°E, even more so. (D) Similar to (B) for the SRC. The darkening of the SRC during year 4 leads to strong variation everywhere. The extra darkening in the region mentioned in (C) leads to stronger variation there.

A small, sharply defined region of several 100 km² at 87°S, 330°E has darkened by close to 0.2 (~25%). The difference in years 2 and 4 SRC albedos appears to have a slight latitudinal gradient, being less further from the pole.

The standard deviations of albedo at each point are also reported in Fig. 3B and D. These values are relatively uncertain as the size of the sample is only three or four numbers; however, they mirror the findings of the previous

figures in terms of which areas are most variable. In addition, they show that the NRC is much more stable in appearance than the surrounding non-icy terrain, whereas the SRC is more variable than its surroundings.

As Bass et al. (2000) found with the Viking dataset, interannual variation in radiometric behavior is difficult to deduce in these views which merge data from a range of seasonal dates. To further investigate interannual

variation, it is also necessary to resolve the seasonal behavior. Fig. 4 shows the evolution of Lambert albedo at selected parallels over ranges of longitude that contain residual ice. The second dimension of the plot is used to represent the time evolution of what is effectively a one-dimensional region.

Two short longitudinal segments of the residual ice from the NRC, to the south and east of the head of Chasma Boreale, are plotted in Fig. 4A and B, respectively. These areas are typical of the stable behavior of the NRC and show mostly repeatable patterns of albedo change. The plots are dominated by the change in albedo caused by the removal of the bright seasonal CO_2 and fine-grained water frost cover at L_s $90°$. Small variations in this defrosting date with location are visible in Fig. 4A–C. These variations are generally repeatable from year to year.

Fig. 4C summarizes the albedo behavior at $87°N$. This parallel intersects several dark bands within the polar cap and other atypical areas. One of the most prominent albedo features at $87°N$ is the bright anomaly at $330°E$. This region is undistinguished while covered with seasonal CO_2 frost; however, it remains bright long after the seasonal CO_2 frost has disappeared. This anomalous behavior has been previously identified in TES data from year 2, by Kieffer and Titus (2001), on the basis of both its high albedo and low temperature. Fig. 4 shows this feature reappears at the same location each year. The anomaly disappears abruptly close to the end of the summer although the exact season varies from year to year in the range of L_s $140–160°$. These data suggest that this feature may be weakening as its longitudinal extent appears to be shrinking. Smaller bright anomalies, such as those at $87°N$, $50–60°E$ and $70–80°E$ during years 2 and 4 are less extensive and appear less consistently.

During year 4, a portion of the NRC at $87°N$, $120–150°E$ was also observed to rapidly darken (see Fig. 4) near the end of the summer at L_s $150°$. This area darkened to a level consistent with ice-free terrain presumably due to sublimation of the large-grained residual ice. This behavior is difficult to understand as this defrosting did not occur in other years. In addition, the albedo of this terrain in the season leading up to its defrosting was slightly higher than in other years, which one would expect to retard sublimation. Again, this change appears easily reversible; water ice persists in that location throughout all seasons in the following year.

There is also considerable structure in the albedo behavior of the seasonal frost, which covers this area. Years 4 and 5 show a repeatable pattern where the seasonal frost suddenly increases in brightness from ∼0.65 to ∼0.75 during the period L_s $30–50°$. After this period the albedo returns to its previous value with equal abruptness. Albedo increases again until the final removal of the seasonal frost close to L_s $90°$. Data covering this period was not available during years 2 and 3; however, year 3 shows some evidence of the return to lower albedos at L_s $50°$. These limited data

suggest that these albedo variations were much less pronounced during that year.

Fig. 4D shows a similar plot for the 3 southern years for which data exist at $87°S$. The albedo of the SRC is almost as high as the seasonal CO_2 frost so there is no obvious drop in albedo as the seasonal CO_2 frost is removed (year 4's anomalous behavior will be discussed below). As has been previously observed (Paige, 1985; James et al., 1992, 2001, Kieffer et al., 2000) the seasonal frost, which covers the residual cap, gets brighter in response to increasing insolation; as the insolation decreases in the latter half of the summer the albedo also decreases. This phenomena remains unexplained but may be related to heating of surface dust grains which can then sublimate ice beneath them allowing the grains to burrow into the ice (James et al., 1992) or microphysical changes in the ice in response to the increased incident energy. The actual emergence of the SRC is different each year. During year 2, the albedo across the cap can be seen to drop slightly at ∼L_s $300–310°$. This effect is more apparent at the margins of the SRC. We interpret this drop to signify the final sublimation of the seasonal frost and exposure of the residual CO_2 ice. In year 3, there appears to be no such distinct drop, i.e. the albedo continues to decrease smoothly with decreasing insolation until the end of the year. The seasonal frost also appears to be brighter during this year. In year 4, not only is the seasonal frost not as bright as in previous years, but also there is an unprecedented large, and sudden, drop in albedo from ∼0.8 to ∼0.65 at all longitudes close to L_s $320°$. This darkening event is the largest interannual difference seen on either of the residual ice caps and may be significant to the long-term viability of the SRC. We will discuss possible explanations in the following section.

Fig. 4 gives an immediate overview of how albedo has varied over large areas and long periods of time. We also examine, in more detail, individual areas that represent both typical and atypical behavior on the residual ice caps.

In the case of the SRC, it is difficult to say what the 'normal' behavior is, as each year is different from the other two in some way. The region at $355–360°E$, $86.9–87°S$ is typical of the SRC as a whole; its behavior is shown in Fig. 5. In contrast, the region at $330–335°E$, $86.9–87°S$ generally has more extreme behavior as identified in Fig. 3; its behavior is shown in Fig. 6. These two regions occupy areas of $95 km^2$ and their positions are indicated in Fig. 1A. In both cases, the yearly albedo behavior is dominated by albedo changes which appear correlated with the solar insolation (which is over-plotted for comparison). In years 2 (∼L_s $310°$) and 4 (∼L_s $320°$), a change occurs whereby the albedo decouples from the decreasing insolation and maintains a nearly constant value (although it still decreases slightly). A sudden drop in brightness, which is more extreme in year 4, also occurs coincident with this. Year 3 does not display this behavior. As mentioned above, albedo continues to decrease smoothly with insolation until the end of the year. The maximum albedo achieved by these regions also varies.
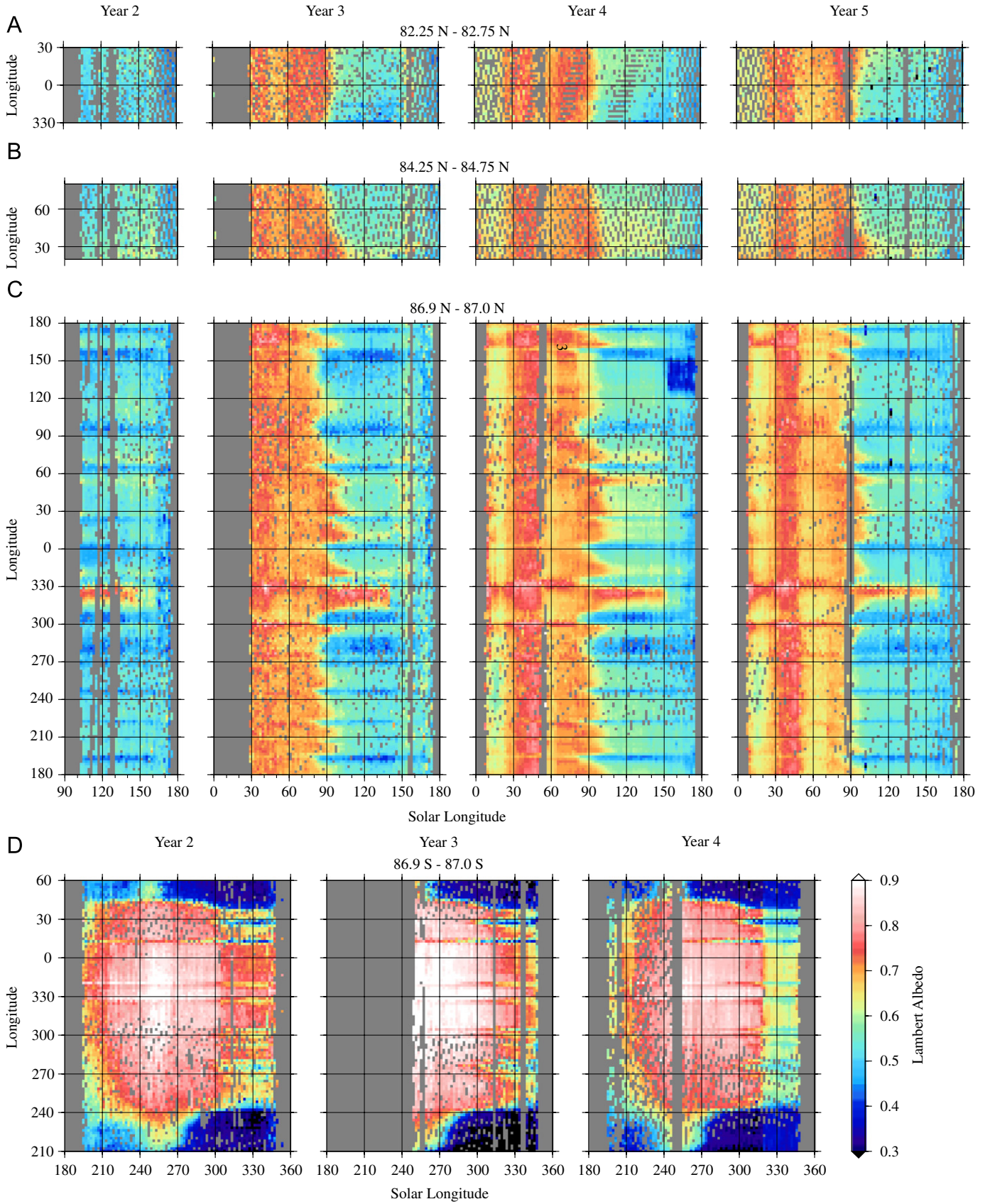
Fig. 4. Lambert albedo changes with season and year for selected latitude bands of interest. Data from L_s 0 to 30° and from L_s 180 to 250° during year 3 are missing due to a solar conjunction and failure of the altimetry mode respectively. See text for discussion.
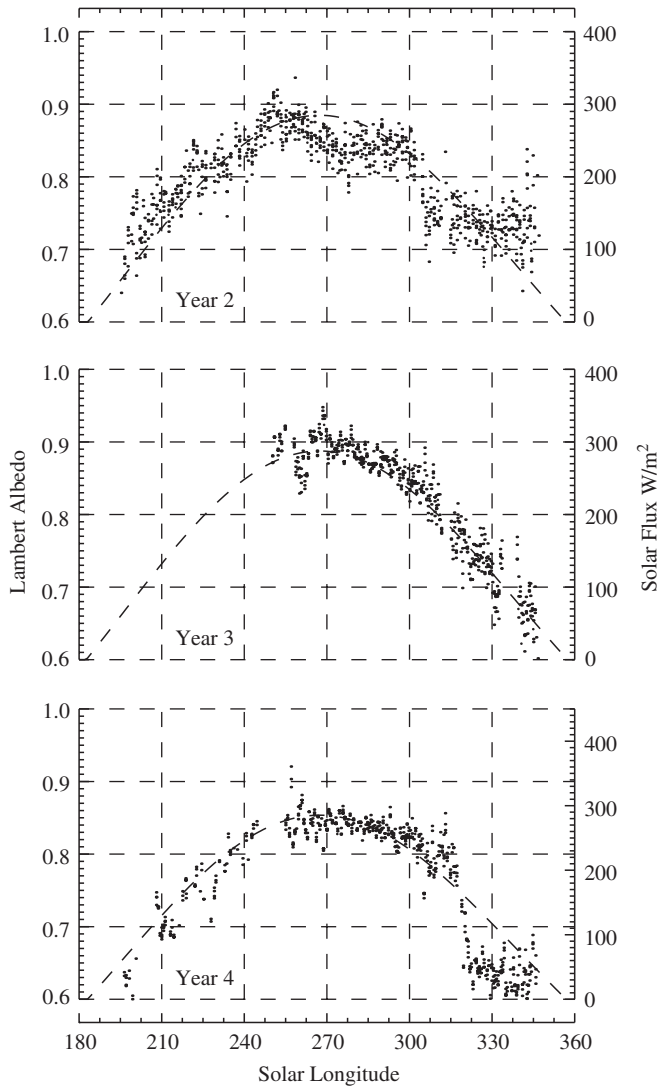
Fig. 5. Seasonal behavior of Lambert albedo in a region of interest on the SRC at 86.9–87°S, 355–360°E (indicated in Fig. 1A). This region exhibits typical SRC behavior. The solar flux on this region has been plotted for comparison (dashed line, right axis). Surface albedo tracks changes in insolation, as has been previously observed in other datasets. See text for discussion.
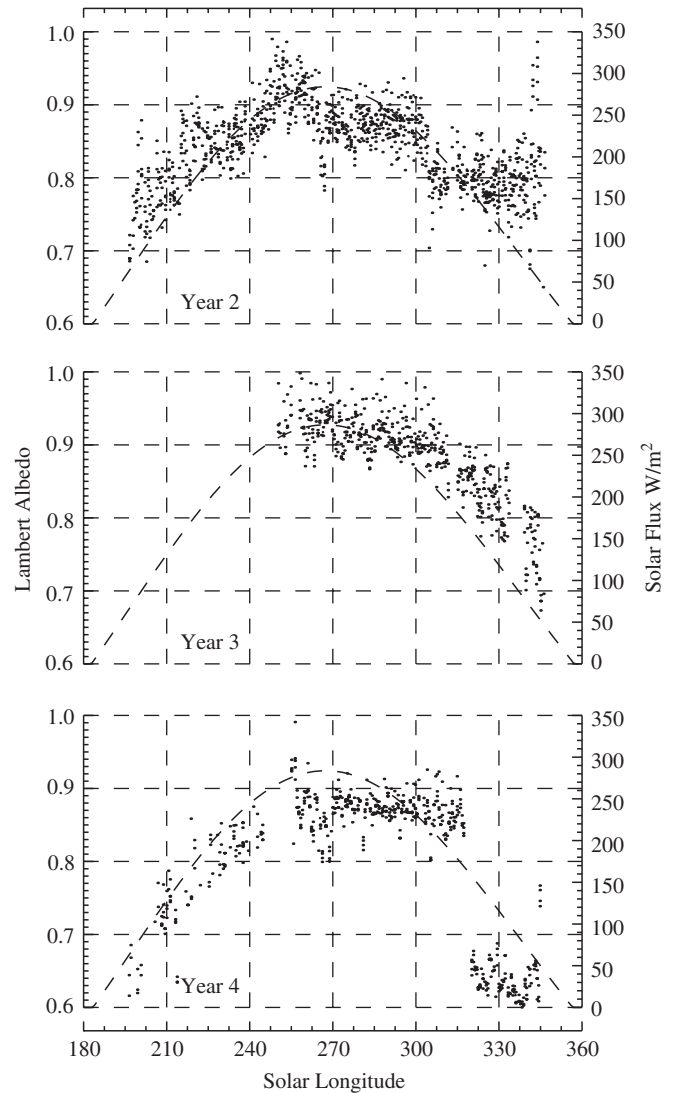
Fig. 6. Seasonal behavior of Lambert albedo in a region of interest on the SRC at 86.9–87°S, 330–335°E (indicated in Fig. 1A). This region exhibits atypical SRC behavior. Its albedo variability is higher than the rest of the SRC due to the extra darkening during year 4. As in Fig. 5, the solar flux on this region has been plotted for comparison (dashed line, right axis). See text for discussion.

Year 3 appears to have reached the highest albedos, although year 2 is almost as high. However, year 4 was 5–10% darker than these previous examples at all times up to L_s 320° (after which it was even darker). The year 2 albedo, close to L_s 270°, undergoes a decrease from which it seems to partially recover. It is possible that a local dust-storm reduced the apparent albedo. The behavior shown in Fig. 6 is basically a more variable version of that which is shown in Fig. 5. This region is usually brighter in general than that just discussed; however, in the darkening event at the end of year 4 they both darken to the same albedo.

For reference, the planet-wide dust-storm of 2001 began close to the beginning of southern summer (L_s 185°) in year 3. Unfortunately, this coincides with the gap in the MOLA data record caused by the altimeter failure. The dust storm had largely abated by the time data collection

recommenced. It is surprising to note that, while dust fallout might have been expected to darken the cap, year 3 was actually the brightest year to date. Reasons for this and other observations presented here will be discussed in the following section.

Figs. 7 and 8 provide a similar perspective for a typical and atypical NRC region, respectively; the locations of these regions are indicated in Fig. 1B. Fig. 7 summarizes the behavior of a typical NRC region at 84.5–85°N, 30–40°E. The unusual albedo behavior of the seasonal CO_2 frost identified in Fig. 5 can be clearly seen here, especially in years 4 and 5. The seasonal frost begins at an albedo of 0.7 and undergoes two cycles of first darkening and then brightening with minima at L_s 20° and 60° (albedos 0.62 and 0.67) and maxima at L_s 40° and 90° (albedo of 0.75). The sharp decrease in albedo from L_s 90–105° to a value of
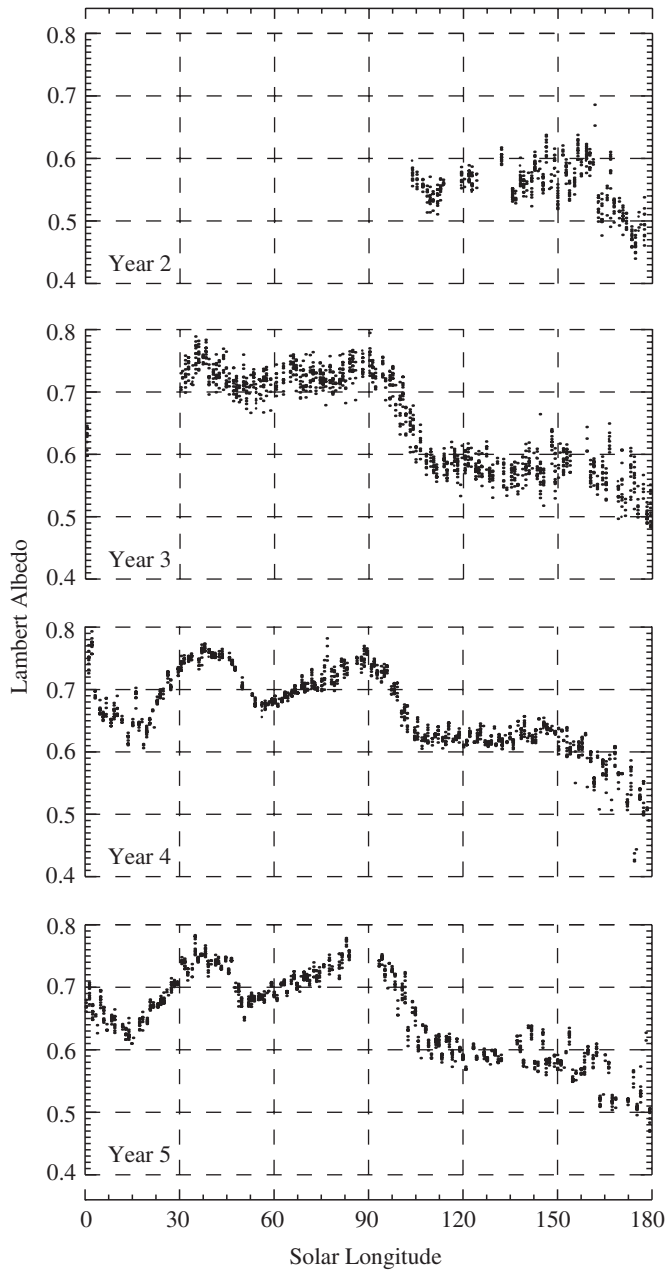
Fig. 7. Seasonal behavior of Lambert albedo in a region of interest on the NRC at 84.5–85°N, 30–40°E (indicated in Fig. 1B). This region exhibits typical NRC behavior. Seasonal frost experiences abrupt (and temporary) decreases in albedo at L_s 15° and 50°, the cap darkens abruptly at $\sim L_s$ 105° due to final sublimation of the seasonal CO_2 and fine-grained water frost. The residual cap albedo decreases slowly over the remainder of the year. See text for discussion.
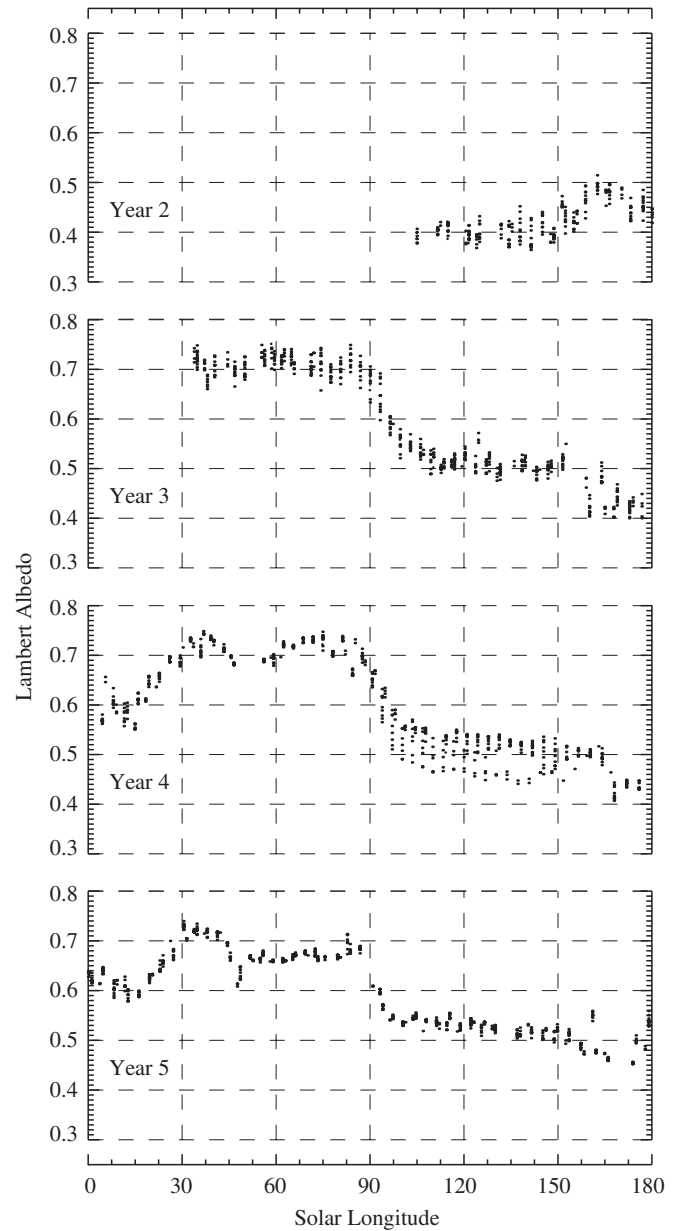
Fig. 8. Seasonal behavior of Lambert albedo in a region of interest on the NRC at 83.5–84°N, 180–185°E (indicated in Fig. 1B). This region exhibits atypical NRC behavior. Seasonal CO_2 frost experiences smaller albedo decreases at L_s 15° and 50°, the cap darkens abruptly at $\sim L_s$ 90° due to final sublimation of the seasonal CO_2 and fine-grained water frost. The residual cap albedo decreases slowly over the remainder of the year. Year 2 exhibits anomalous behavior in that the residual cap seems to have fully defrosted during that year and the region subsequently brightened as the year progressed. See text for discussion.

0.6 is due to the final sublimation of the seasonal CO_2 and bright water frost (which tracks the retreating edge of the CO_2 cap) and exposure of the darker residual cap.

The NRC in year 4 appears brighter than those of other years. Again this seems counter-intuitive regarding the timing of the 2001 dust storm. During the dust-storm, in the second half of year 3, the north polar seasonal cap was formed. One might expect more than the usual amount of dust to be incorporated into this seasonal ice. During the

summer in the following year one may also expect that this sublimating CO_2 will leave behind a dirtier residual cap; however, the opposite seems to have occurred.

Fig. 7 shows that the NRC albedo is quite stable over the course of the summer. However, its albedo does show a marked downward trend (by about 20%) in the period L_s 150–180°. This late-summer darkening trend repeats robustly each year. We offer a model to explain this late-summer darkening in the following section.

Fig. 8 summarizes the behavior of an atypical NRC region at 83.5–84°N, 180–185°E. This region was previously identified as highly variable (Fig. 3), and appears to have defrosted completely during year 2. Fig. 8 shows a less prominent version of the same unusual seasonal frost behavior for Fig. 7 discussed above. The slightly lower latitude results in a slightly earlier defrosting date. In years 3–5, the same late-summer darkening occurs with residual cap albedos decreasing by about 20%. However, year 2 residual cap albedos are considerably lower. The defrosting period for this year was not observed, data coverage begins at ~L_s 105°, just after the seasonal frost would have been expected to finish sublimating. Rather than start at a high value and slowly decrease, the albedo for this year begins at a low value and slowly increases.

For comparison with the NRC, we show the seasonal albedo behavior of Korolev crater in Fig. 9. Korolev contains residual ice but is relatively far from the pole (centered at 72.75°N). Its albedo variation is quite different from the main NRC. After the seasonal CO_2 and water frost has fully sublimated (L_s 80°) the albedo is close to 0.52. During the rest of the summer, the albedo increases to about 0.62 at L_s 120° and maintains that value until L_s 150° after which Korolev darkens again to close to 0.5. Korolev's non-polar location means the data are sparser both temporally and spatially, especially in year 4. The wide spread of albedo values at each L_s indicates non-uniform conditions within the crater which may be due to differing local slopes.

In the preceding discussion we have treated these surfaces as diffuse reflectors and discussed only their Lambert albedos. Such an approach is valid when looking for interannual changes in reflectance as only observations with like-geometry are compared. Here, we investigate the degree to which these deposits depart from diffuse behavior. We fit the widely used model of Hapke (1993) to our bi-directional reflectance measurements. The model bidirectional reflectance is given by Eq. (3), where w is the single scattering albedo of the particles and μ and μ_0 are the cosines of the emission and incidence angles, respectively:

$$r = \left(\frac{w}{4\pi}\right)\left(\frac{\mu_0}{\mu + \mu_0}\right)[P(g) + H(\mu)\,H(\mu_0) - 1]. \tag{3}$$

We neglect the term describing the opposition effect (not shown) as the phase angle is always greater than 50° in our observations of the residual caps. Also, Hapke's treatment of surface roughness does not account for radiation scattered from surface element to surface element, and so is less accurate for higher albedo surfaces such as these icy deposits. For this reason, this term has also been ignored. $H(x)$ are the isotropic scattering functions of Chandrasekhar (1960). We use a somewhat unconventional approximation to these non-linear integrals given by Eq. (4):

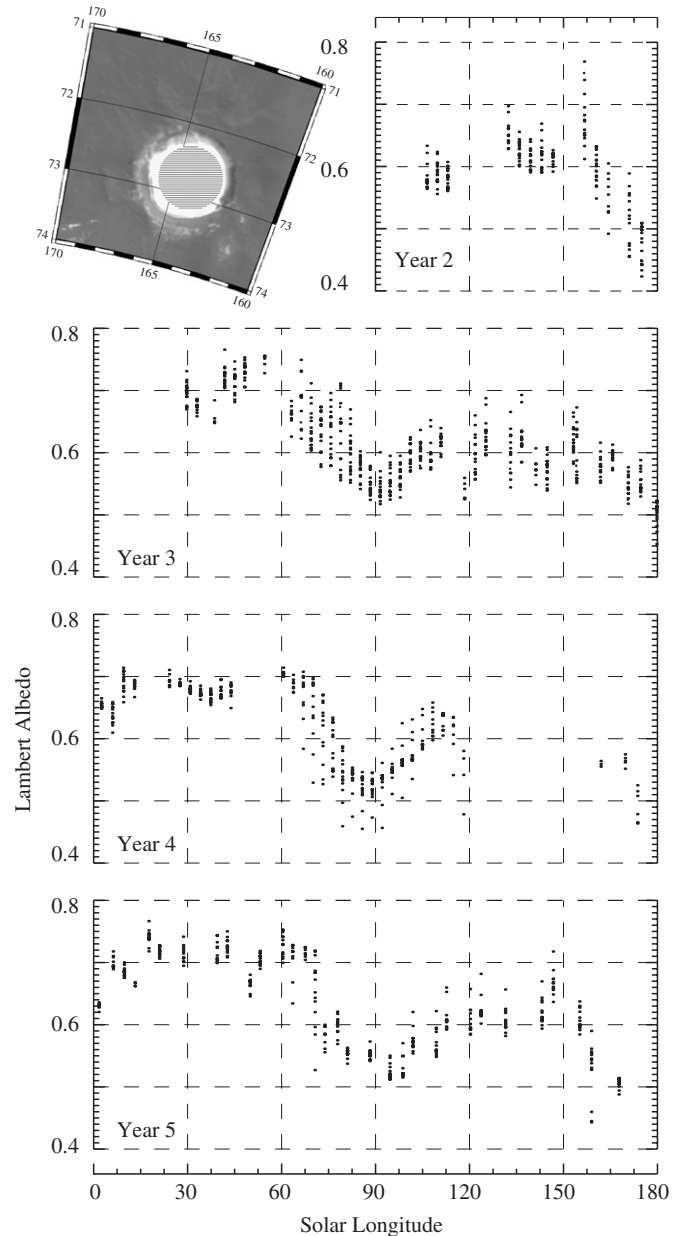$$H(x) = \frac{1}{1 - (1 - \gamma)x[r_0 + (1 - (r_0/2) - r_0 x)\,\ln((1 + x)/x)]}, \tag{4}$$

Fig. 9. Seasonal behavior of Lambert albedo in Korolev crater, context image from MOC wide angle atlas. Albedo values are taken from the lined region centered on 72.75°N, 164.3°E (radius 0.45°). Residual ice displays behavior very distinct from the main NRC. See text for discussion.

where

$$\gamma = \sqrt{1 - w}, \qquad r_0 = \frac{1 - \gamma}{1 + \gamma}.$$

Although more complex than the usual formulation, this approximation (from equation 8.57 of Hapke (1993)) provides a more accurate estimation of $H(x)$ for extremely bright surfaces. $P(g)$ is the surface phase function which we approximate with a double-lobed Henyey–Greenstein function given by Eq. (5), where g is the phase angle, k is the asymmetry factor and f is the weighting

of forward vs. backward scattering:

$$P(g) = (1-f)\left\{\frac{1-k^2}{[1-2k\,\cos(g)+k^2]^{3/2}}\right\}$$
$$+ f\left\{\frac{1-k^2}{[1+2k\,\cos(g)+k^2]^{3/2}}\right\}. \quad (5)$$

A diffusely scattering surface would have a k of 0 leading to $P(g) = 1$ for all phase angles; the larger the value of k (up to a maximum value of 1), the more the surface departs from diffuse behavior. For non-isotropically scattering surfaces f describes the scattering direction. An f value of 0 indicates predominantly forward-scattering behavior, whereas a value of 1 would indicate the opposite.

We considered a sample area from the northern (82–83°N, 0–10°E), and southern (86.9–87°S, 345–355°E) residual ice caps. We chose seasonal ranges where we would expect the residual caps to be exposed and fit the model to each year's data separately. In the northern case, where the region of interest was not at latitude 87°, we included only points on daytime passes of the MGS spacecraft. Given the observational geometry of these points, we first solved the forward problem to produce modeled bidirectional reflectances. These were compared to the measured values and the quality of the fit for the model parameters used was evaluated. To find the best fit values for these parameters we explored the whole of parameter space at low resolution, i.e. repeatedly solved the forward problem for all the data points using different values of k, f and w. Regions of parameter space surrounding the best-fit values were examined in successively higher resolution until the best-fit values were determined to within a part in 400.

Our best-fit values for each parameter are shown in Table 2. The Hapke model fits are shown in Fig. 10. In general, this model describes the data well; however, the unrealistically high reflectances over the polar caps make the fit values of the single scattering albedo suspect. We can still use these data to examine the best-fit phase behavior, however, as that is a measure of relative brightness in different geometries. As previously mentioned our range of observing geometries is quite limited and consequently the scattering behavior is only constrained over this small range. We can still distinguish between differing scattering
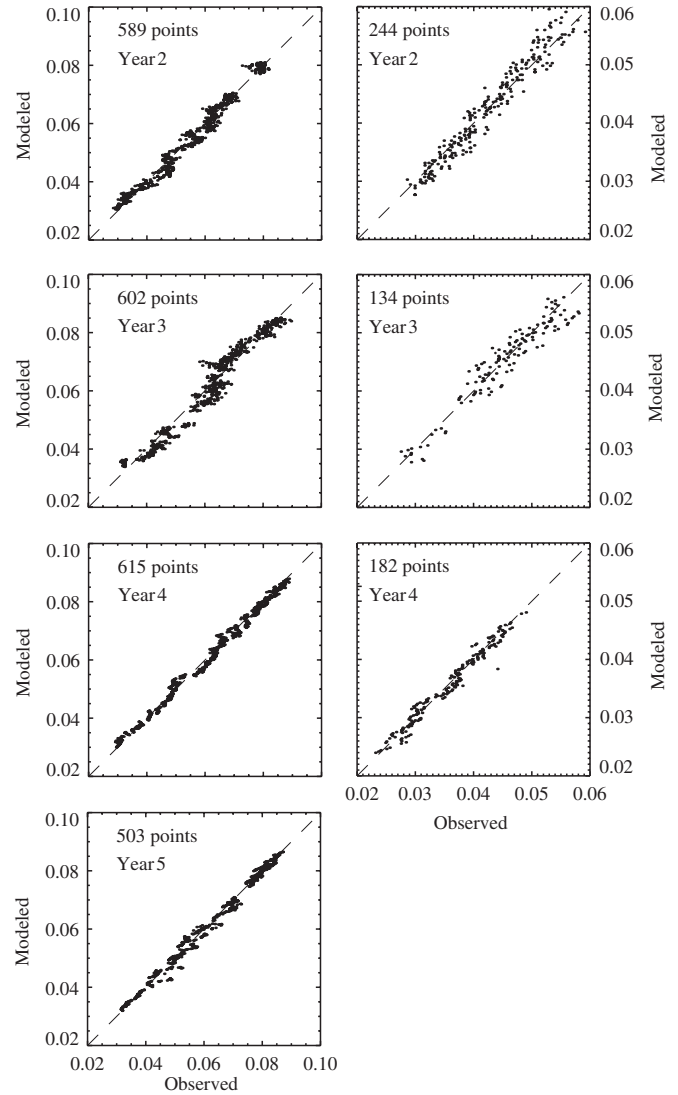

Fig. 10. Fits of the Hapke scattering model to bidirectional reflectance measurements within regions of interest on the northern (82–83°N, 0–10°E), and southern (86.9–87°S, 345–355°E), residual ice caps. Modeled bidirectional reflectance values are plotted against our observations. The model parameters resulting from these fits can be found in Table 2.

behaviors over this range, even though the parameters reported in Table 2 are probably not appropriate for very high or low phase angles.

The NRC region shows different scattering behavior for different years. Years 2 and 3 show only small departures from isotropic scattering. The non-isotropic scattering in year 2 occurs in both the forward and backward directions (at the expense of phase angles near 90°). The NRC in year 3 appears to scatter virtually isotropically. Years 4 and 5 show remarkably consistent behavior. Both fits indicate a strongly backscattering surface. The difference between years 2–3 and 4–5 is unlikely to be due to the reconfiguration of the instrument, as the scattering properties of the SRC (discussed below) appear to have been unaffected by the change. The change in scattering parameters thus appears to represent some real change in the surface

Table 2
Hapke model parameters derived from residual cap bidirectional reflectance

Year	SRC			NRC		
	w	k	f	w	k	f
2	1.000	0.485	0.000	0.9475	0.320	0.475
3	1.000	0.470	0.000	0.9525	0.035	0.000
4	0.975	0.235	0.525	0.9775	0.720	1.000
5	–	–	–	0.9775	0.750	1.000

SRC area is 345–355°E, 86.9–87°S, and L_s 325–340°; NRC area is 0–10°E, 82–83°N, and L_s 120–170°.

properties that occurred between years 3 and 4. It is also possible that years 2 and 3 were influenced by some atmospheric activity that did not occur in years 4 and 5 (or vice versa); however, it seems unlikely that a variable atmospheric phenomenon would repeat in that pattern. One final (and less likely) possibility is that the changes were caused by the change in spatial resolution of our observations between years 3 and 4. As previously mentioned, the NRC appears extremely homogenous so it is unclear how a resolution change would affect the scattering properties of the surface.

In contrast to the NRC, mapping and extended mission data from the SRC region agree well. Years 2 and 3 indicate that the SRC scatters light predominantly in the forward direction. The agreement between fits derived from data taken in these 2 years is close, despite the fact that the observational and instrument parameters had changed in the interim. The final year in the SRC record indicates a distinct difference in the scattering properties from previous years. The residual cap is now only scattering light in a slightly non-isotropic manner in both the forward and backward directions, similar to the behavior of the NRC in year 2. This is consistent with the previously discussed brightness observations, showing that the SRC this year darkened abruptly at L_s 320°, and points to scattering dominated by a different kind of particle (either in size or composition). Possible reasons for this darkening and change in scattering properties will be discussed in the following section.

4. Discussion and conclusions

The extent of the SRC appears stable in each observed year, consistent with results reported by Benson and James (2005). However, the NRC exhibits several areas of change discussed in the previous section. These areas are generally small compared to the total NRC area and show anomalous changes in albedo on only one of the 4 observed years. Thus, interannual changes in NRC extent appear to be minor and quickly reversible and so are unlikely to have a significant effect on current climatic parameters such as the water-vapor budget.

The distinctive albedo oscillations of the northern cap, seen in Fig. 7, can be explained in a qualitative way. A decrease in the grain size within the seasonal CO_2 ice can result in the first increase in albedo observed from L_s 15–40°. Recent atmospheric modeling (Colaprete et al., this issue) suggests that deposition of fresh, fine-grained, CO_2 ice occurs in an annulus just within the edge of the retreating seasonal CO_2 cap. As the seasonal cap retreats poleward this annulus of fine-grained (and consequently bright) frost deposition sweeps past the location represented in Fig. 7. Once this bright annulus has passed the albedo decreases again, upon final sublimation of the CO_2 frost, as the edge of the seasonal CO_2 cap moves through the observed region.

The second albedo increase, from L_s 50 to 90°, is primarily due to water frost, an annulus of which also

tracks the edge of (but in this case is external to) the seasonal CO_2 cap. A band of water frost, external to the edge of the seasonal CO_2 cap, had been expected from previous modeling, e.g. Houben et al. (1997). This bright, but non-CO_2, component of the seasonal cap has been identified both thermally from the TES instrument (Titus, 2005; Kieffer and Titus, 2001) and spectrally from the OMEGA instrument (Langevin et al., 2005). This seasonal water frost disappears to reveal the large-grained, and consequently darker, NRC close to L_s 105°. The albedo of the NRC remains stable throughout the rest of the summer until L_s 155°, when it begins a darkening trend that will persist until the end of the year.

The thickness of this northern residual ice cover remains an open question. The unusual surface texture shown in Fig. 1E obviously has some relief; knowledge of that relief would place a lower limit on the residual ice thickness. Here, we show how the late-summer darkening observed over the residual ice (e.g. Fig. 7) can be used to estimate this quantity.

A possible explanation for the steady darkening of the NRC during the end of the summer is lengthening of shadows within its rough topography. To a nadir observer the shadow length is given by $h^* \tan(i)$, where h is the magnitude of the relief casting the shadow and i is the incidence angle. As the incidence angle increases at the end of the summer the terrain would be expected to darken even if its intrinsic albedo remained constant. We can roughly estimate the relief of the shadow-generating topography by using a simplified topographic model.

We approximate the NRC surface texture as a checkerboard pattern of alternating high and low elevation. Areas of high topography are square and bounded on all four sides by low regions and vice versa. We will assume that both high and low areas have the same albedo (A_t), which does not change with time. A cross-section of this topography appears in cartoon form in Fig. 11. We will also ignore light scattered from atmospheric particles and approximate the observed albedo (A_0) as a linear mix of the true surface albedo (A_t) and the effective albedo of shadowed regions ($c^* A_t$), where c may be thought of as the ratio of the diffuse to the total insolation. Shadowed regions are not completely dark, (i.e. $c \neq 0$) as radiation can be scattered into these areas from both the atmosphere and surrounding surfaces which are illuminated. Indeed, the high albedo of the residual ice means light scattered into shadows from nearby illuminated surfaces may be significant. Using the geometry represented in the cartoon in Fig. 11 and the above assumptions, we can write down an expression for the observed albedo.

$$A_o = \left\{ \frac{2x^2 - hx \tan(i)[\cos(\phi) + \sin(\phi)] + h^2 \tan^2(i) \cos(\phi) \sin(\phi)}{2x^2} \right\} A_t$$
$$+ \left\{ \frac{hx \tan(i)[\cos(\phi) + \sin(\phi)] - h^2 \tan^2(i) \cos(\phi) \sin(\phi)}{2x^2} \right\} c A_t,$$
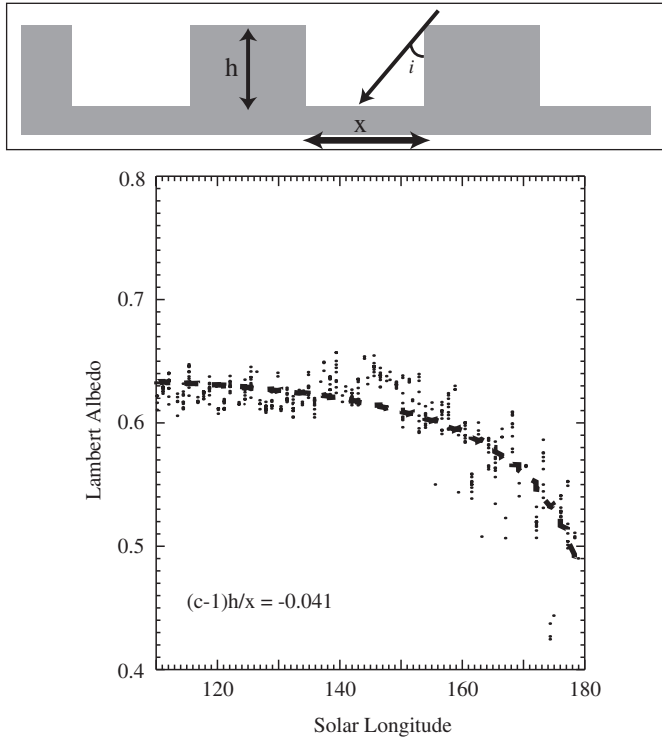
(6)

Fig. 11. Cartoon of shadowing within the NRC. The amplitude of the topography can be estimated in this simplified geometry. Lower plot shows a subset of data in Fig. 7 for year 4 with dashed line representing a best-fit of the simple shadowing model.

where φ is the azimuth of the Sun ($0°$ and $90°$ along the checkerboard edges). We can assume that the individual pits are randomly orientated and so use the mean values for the terms including φ in Eq. (6). These mean values are given by Eq. (7):

$$\frac{\int_0^{\pi/2} [\cos(\phi) + \sin(\phi)]\,d\phi}{\int_0^{\pi/2} d\phi} = \frac{4}{\pi} \quad \text{and}$$

$$\frac{\int_0^{\pi/2} \cos(\phi)\,\sin(\phi)\,d\phi}{\int_0^{\pi/2} d\phi} = \frac{1}{\pi}. \tag{7}$$

Substituting Eq. (7) into Eq. (6) and rearranging gives the following expression:

$$A_o = A_t + \left[A_t(c-1)\left(\frac{h}{x}\right)\frac{2}{\pi}\right]\tan(i)$$
$$- \left[A_t(c-1)\left(\frac{h}{x}\right)^2 \frac{1}{2\pi}\right]\tan^2(i), \tag{8}$$

It can be seen from Eq. (8) that, under this model, the observed albedo, A_o, should vary quadratically with $\tan(i)$. However, the quadratic term is likely to be small as it depends on the square of (h/x), and we only consider data where the incidence angle is less than $84°$ ($\tan(i) < 10$). As there are many other shortcomings of such a conceptually simple model we will ignore the quadratic term, it represents a small deviation from what is mostly linear

behavior and its inclusion will not improve accuracy. A linear fit between A_o and $\tan(i)$ was performed using a subset of the data shown in year 4 in Fig. 7 (only L_s $110–180°$ were included). The ratio of the derived slope to the intercept is given by $(c-1)(h/x)(2/\pi)$, independent of the actual surface albedo. For $c = 0$, i.e. shadows are completely dark, h/x was found to be 0.041 indicating that the topography has an aspect ratio close to 25:1. The length-scale (x) of the individual high/low patches shown in Fig. 1(E) is of order 20 m leading to an estimate of the topographic relief of order 80 cm.

Fig. 11 shows how this model fits these data; although the model is simplistic the agreement is good. As c increases the relief required to generate the same darkening effect also increases, for c values of 0.1, 0.2 and 0.3, the topographic aspect ratios decrease to 22:1, 19:1 and 17:1 leading to relief estimates of order 92, 104 and 118 cm. Higher values of c seem unlikely; the approximate nature of this model makes a rigorous calculation of this parameter pointless. The reader may note that, by including the quadratic term in the model fit, an unambiguous value of (h/x) may be obtained from the ratio of the coefficients of the linear and quadratic terms. Unfortunately, in practice, the coefficient of the quadratic term is poorly constrained by these data. The spread in albedo measurements within the region is sufficient to obscure any non-linearity, leaving only the dominant linear trend being well constrained.

Thomas et al. (2000) used the lack of shadows at L_s $120°$ to constrain NRC relief to be less than 2 m. What this observation actually constrains, however, are the typical slopes which, combined with a length scale, can constrain the relief. Fig. 11 shows that the late-summer darkening begins at about L_s $150°$. So long as the typical slopes are high enough to cast shadows in the time-span L_s $150–180°$ then the solution discussed above remains appropriate. Factors other than shadows may also affect the seasonal evolution of the NRC albedo. Ice-grain growth can lower the albedo (Kieffer, 1990; Langevin et al., 2005; Bass et al., 2000) as can accumulation of atmospheric dust. No effort is made here to take these factors into account. In addition, the model presented does not include a rigorous treatment of atmospheric scattering and treats the surface topography extremely simply. We have approximated the diffuse flux which illuminates shadows and reduces contrast between shadowed and unshadowed areas as a constant fraction of the direct flux when in reality this quantity changes with atmospheric conditions and incidence angle.

Despite these reservations, if the darkening observed is due to shadowing, then the figure of 80 cm quoted above for the $c = 0$ case should be a robust lower bound on the topographic relief. If this topography does not penetrate below the residual cap into the underlying layered deposits then this number is also a lower limit on the thickness of the residual cap. It is worth noting that this limit applies only to this region of the NRC. Although the NRC appears homogenous in MOC narrow angle images, the

thickness of this deposit may still vary from place to place. Topography generated from stereo imaging is usually limited in resolution to be several times coarser than that of the images themselves, making measurements of these small features difficult. Similarly, topography retrieved from shading (photoclinometry) cannot be reliably applied in cases where shadows are cast. Stereo imaging from a higher resolution camera such as the upcoming HiRISE instrument on the Mars Reconnaissance Orbiter may further constrain this small-scale topography.

The seasonal behavior of the SRC albedo is dominated for much of the year by the apparent dependence of albedo on incident solar radiation (see Fig. 5). However, as mentioned in the previous section, Fig. 5 shows that in years 2 and 4 there is a distinct break in the downward albedo trend close to L_s 310–320°. Albedo, in these cases, maintains a roughly constant value for the rest of the year. The late-summer albedo in year 3 shows no such break and decreases smoothly with insolation until the end of the year. We interpret these observations to mean that this insolation-dependant albedo behavior is a property of the seasonal frost but not of the residual CO_2 ice, which likely has a different grain-size and density. Years 2 and 4 completely lose their seasonal cover before the polar sunset, resulting in net ablation of the residual deposit. However, the behavior of year 3 indicates that the residual CO_2 ice was never actually exposed, i.e. there was sufficient seasonal CO_2 frost present to last through the entire year. This is consistent with the higher maximum albedos achieved during the summer, which may indicate greater seasonal frost coverage; indeed, the higher albedos may be the reason for the seasonal frost's survival. Much attention has recently focused on the possibility that the Mars' solid CO_2 reservoir is currently dwindling both from ablation of CO_2 landforms within the boundaries of the cap (Malin et al., 2001) and possible retreat of its outer margins (Titus et al., 2003). This interpretation of these albedo data, i.e. that net deposition of CO_2 occurred during at least one year, may remove the difficulty of why such an apparently quickly shrinking SRC is present for us to observe at all. The reason behind year 3's behavior is unclear, it may be that this year is typical and years 2 and 4 are less usual. The current observational record is not yet long enough to permit statements of that nature.

The darkening of the SRC in year 4 is the most striking example of interannual variability within our current record. Fig. 4 illustrates that this darkening occurred simultaneously throughout the SRC. In most regions this darkening process spanned a few (~5) degrees of L_s (e.g. Fig. 5); in less typical areas the darkening process took only hours (e.g. Fig. 6). To assess the impact of this event on the stability of the SRC, it is necessary to know whether the cause is a true darkening of the surface or due to interaction of reflected light with particles suspended in the atmosphere. Dust suspended in the atmosphere tends to drive the apparent albedo toward that of the dust itself, i.e. it will brighten dark surfaces and darken bright surfaces.

Similarly, the apparent scattering phase function will depart from that of the surface and approach that of the dust as more photons are scattered by these aerosols. Thus, the changes in the scattering behavior could also be at least partly due to atmospheric dust.

Unfortunately, the retrieval algorithm used to derive atmospheric optical depths (Smith et al., 2000) cannot be used when the surface is colder, or as cold, as the atmosphere. The residual caps are cold enough that valid optical depth measurements are not available for the overlying atmosphere at any time. The SRC darkening takes place sufficiently late in the summer (L_s 320°) that near-cap terrain is also too cold to retrieve the overlying optical depth. We can, however, examine the reasonableness of the SRC darkening being due to atmospheric scattering.

We examined the dependence of the apparent albedo on atmospheric optical depth and incidence angle by using results from the plane-parallel radiative-transfer model, DISORT (Stamnes et al., 1988). Dust was considered to be the only scattering aerosol, the optical properties of which were taken from analysis of the Pathfinder imaging data (Tomasko et al., 1999). The model results were provided by Mike Wolff (Space science Institute, personal communication); see Wolff and Clancy (2003) for a description of how the model was implemented.

In Fig. 12, we show a summarized version of these model runs, for the incidence angle of interest (76°) for this location and season. It can be seen that the apparent brightness of a surface with a Lambert albedo of 0.8 is extremely sensitive to the optical depth of the atmosphere. To match the observations, i.e. drop the albedo from 0.8 to 0.65, an optical depth of only 0.15 is required. In contrast, the terrain surrounding the SRC is observed to have an albedo of 0.3, which appears roughly constant regardless of the optical depth. These results demonstrate that the
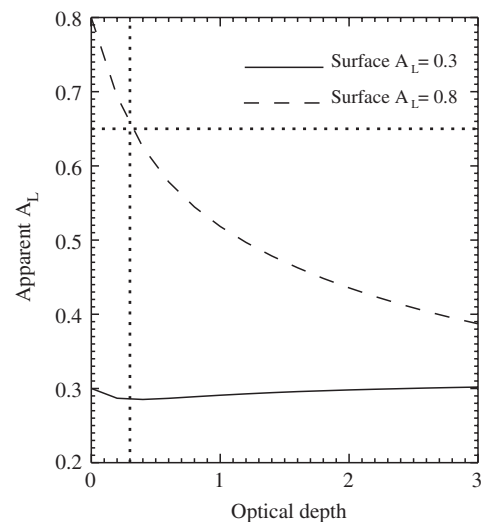

Fig. 12. Plot of Lambert albedo deduced by an observer above the atmosphere as a function of atmospheric extinction optical depth at 1064 nm. Plotted for true surface albedos of 0.8 (dashed) and 0.3 (solid).

introduction of a modest amount of atmospheric dust could reproduce the observed SRC darkening. In addition to this, examination of albedo and optical depth information over the mid-latitudes in the southern hemisphere shows that a large dust storm did indeed begin at this time. This dust appeared to quickly spread southward, although as previously mentioned we cannot examine the optical depth over the polar area itself. Thus, it appears from this circumstantial evidence, coupled with the effectiveness of dust at reducing the cap's apparent albedo, that the year 4 SRC darkening is most likely due to atmospheric scattering. As mentioned above, this atmospheric dust is at least partly responsible for the change in scattering properties. This increased atmospheric optical depth likely resulted in higher sublimation rates of the SRC due to increased downwelling infrared radiation. The seasonal lateness of this event however, meant that the survival of the residual CO_2 deposit was not threatened.

While this SRC darkening event is unusual, in that it does not occur in the other observed years, it is again worth bearing in mind that 3 years is not a long record. An event that happens in one of three cases could hardly be considered rare. Unfortunately, patience is required to acquire a longer record and so better constrain how common this kind of event, or that of the unusually bright year 3, may be. It is likely that year 5 (observations currently being acquired) will show a brighter residual cap during this period; however, the seasonal frost may be both thinner and darker due to the extra energy deposited at the end of year 4 and the subsequent dust fallout.

Finally, it is interesting to consider what effect, if any, the 2001 planet-wide dust storm may have had on the residual ice caps and the seasonal frost which covers them. The results of such an inquiry are counter-intuitive. The dust storm began at L_s 185° in year 3. The evolution of this storm is discussed in detail by Smith et al. (2002). It suffices to say here, that it became plant-encircling within 2 weeks and quickly spread to all latitudes. While this storm was taking place, the year 3 appearance of the SRC was just beginning. One may expect the dust fallout to darken the seasonal frost covering the residual cap; however, year 3 was the brightest appearance of the cap in our record (Fig. 5). This higher albedo may be what is responsible for the survival of seasonal CO_2 over the SRC until the end of the year, which we earlier inferred from the persistence of the insolation dependence of its albedo. Over the NRC, seasonal frost, which would be later exposed and sublimated during year 4, was beginning to form. One may also expect increased amounts of dust to be incorporated into this seasonal deposit. In fact, year 4 also proved to have the brightest seasonal and residual northern ice cap albedos (Fig. 7). These counter-intuitive results are consistent with the work of Benson and James (2005), who showed the 2001 dust-storm had no effect on the recession rate of the seasonal caps. This may perhaps be explained by the increased atmospheric activity, generated by heating of atmospheric dust. The polar vortex in both hemispheres isolates the polar caps from the rest of the atmosphere. A dustier atmosphere at this season may generate a stronger polar vortex, which, ironically, may result in seasonal ice, which incorporates less dust. The NRC scattering properties did exhibit a change (see Table 2) between years 3 (pre-storm) and 4 (post-storm). This may be due to dust deposition on the residual ice; however, this is inconsistent with the albedos just mentioned.

Assessing the seasonal and interannual variability of the Martian polar caps is becoming more reliable and informative as our observational record grows longer. Continuous spacecraft monitoring now looks likely for the foreseeable future. Any current deposition of polar layered deposits occurs through the residual ice caps. Understanding the long-term (in)stability of the current residual ice caps is an important step in the understanding the formation of the polar layered deposits. Thus, observations of the kind discussed in this paper will hopefully contribute to the long-term goal of inferring Martian climatic history through the polar layered deposits.

References

Abshire, J.B., Sun, X., Afzal, R.S., 2000. Mars Orbiter Laser Altimeter: receiver model and performance analysis. Appl. Opt. 39, 2449–2460.

Aharonson, O., Zuber, M.T., Rothman, D.H., 2001. Statistics of Mars' topography from the Mars Orbiter Laser Altimeter: slopes, correlations, and physical models. J. Geophys. Res. 106, 23723–23736.

Albee, A.L., Palluconi, F.D., Arvidson, R.E., 1998. Mars Global Surveyor Mission: overview and status. Science 279, 1671.

Albee, A.L., Arvidson, R.E., Palluconi, F., Thorpe, T., 2001. Overview of the Mars Global Surveyor Mission. J. Geophys. Res. 106, 23291–23316.

Bass, D.S., Herkenhoff, K.E., Paige, D.A., 2000. Variability of Mars' North Polar water ice cap. I. Analysis of Mariner 9 and Viking Orbiter Imaging Data. Icarus 144, 382–396.

Bell, J.F., Wolff, M.J., James, P.B., Clancy, R.T., Lee, S.W., Martin, L.J., 1997. Mars surface mineralogy from Hubble Space Telescope imaging during 1994–1995: observations, calibration, and initial results. J. Geophys. Res. 102, 9109–9124.

Bell, J.F., Wolff, M.J., Daley, T.C., Crisp, D., James, P.B., Lee, S.W., Trauger, J.T., Evans, R.W., 1999. Near-infrared imaging of mars from HST: surface reflectance, photometric properties, and implications for MOLA data. Icarus 138, 25–35.

Benson, J.L., James, P.B., 2005. Yearly comparisons of the Martian polar caps: 1999–2003 Mars Orbiter Camera observations. Icarus 174, 513–523.

Bibring, J.-P., et al., 2004. Perennial water ice identified in the south polar cap of Mars. Nature 428, 627–630.

Byrne, S., Ingersoll, A.P., 2003. A sublimation model for Martian south polar ice features. Science 299, 1051–1053.

Calvin, W.M., Titus, T.N., 2004. Summer season variability of the north residual cap of Mars from MGS–TES. Lunar Planetary Inst. Conf. Abstr. 35, 1455.

Caplinger, M.A., Malin, M.C., 2001. Mars Orbiter Camera geodesy campaign. J. Geophys. Res. 106, 23595–23606.

Chandrasekhar, S., 1960. Radiative Transfer. Dover, New York.

Christensen, P.R., Anderson, D.L., Chase, S.C., Clark, R.N., Kieffer, H.H., Malin, M.C., Pearl, J.C., Carpenter, J., Bandiera, N., Brown, F.G., 1992. Thermal Emission Spectrometer experiment—Mars observer mission. J. Geophys. Res. 97, 7719–7734.

Christensen, P.R., et al., 2001. Mars Global Surveyor Thermal Emission Spectrometer experiment: investigation description and surface science results. J. Geophys. Res. 106, 23823–23872.

Clifford, S.M., et al., 2000. The state and future of Mars polar science and exploration. Icarus 144, 210–242.

Colaprete, A., Barnes, J.R., Haberle, R.M., Hollingsworth, J.L., Kieffer, H.H., Titus, T.N., 2005. Albedo of the south pole on Mars determined by topographic forcing of atmosphere dynamics. Nature 435, 184–188.

Colaprete, A., Haberle, R.M., Barnes, J.R., Montmessin, F., this issue. CO_2 clouds. CAPE and convection: observations and general circulation modeling. Planet. Space Sci., doi:10.1016/j.pss.2007.08.010.

Cutts, J.A., 1973. Nature and origin of layered deposits of Martian polar regions. J. Geophys. Res. 78 (20), 4231–4249.

Hale, A.S., Bass, D.S., Tamppari, L.K., 2005. Monitoring the perennial Martian northern polar cap with MGS MOC. Icarus 174, 502–512.

Hapke, B., 1993. Theory of Reflectance and Emittance Spectroscopy. Cambridge University Press, New York.

Houben, H., Haberle, R.M., Young, R.E., Zent, A.P., 1997. Modeling the Martian seasonal water cycle. J. Geophys. Res. 102, 9069–9084.

Jakosky, B.M., Haberle, R.M., 1990. Year-to-year instability of the Mars south polar CAP. J. Geophys. Res. 95, 1359–1365.

James, P.B., Martin, L., 1985. Interannual water loss by Mars' north polar cap. Bull. Am. Astron. Soc. 17, 735.

James, P.B., Briggs, G., Barnes, J., Spruck, A., 1979. Seasonal recession of Mars' south polar cap as seen by Viking. J. Geophys. Res. 84, 2889–2922.

James, P.B., Kieffer, H.H., Paige, D.A., 1992. The seasonal cycle of carbon dioxide on Mars. In: Kieffer, H.H., Jakosky, B.M., Snyder, C.W., Matthews, M.S. (Eds.), Mars. University of Arizona Press, pp. 934–968.

James, P.B., Cantor, B.A., Davis, S., 2001. Mars Orbiter Camera observations of the Martian south polar cap in 1999–2000. J. Geophys. Res. 106, 23,635–23,652.

James, P.B., Bonev, B.P., Wolff, M.J., 2005. Visible albedo of Mars' south polar cap: 2003 HST observations. Icarus 174, 596–599.

Kieffer, H.H., 1979. Mars south polar spring and summer temperatures— a residual CO_2 frost. J. Geophys. Res. 84, 8263–8288.

Kieffer, H.H., 1990. H_2O grain size and the amount of dust in Mars' residual north polar CAP. J. Geophys. Res. 95, 1481–1493.

Kieffer, H.H., Titus, T.N., 2001. TES mapping of Mars' north seasonal cap. Icarus 154, 162–180.

Kieffer, H.H., Martin, T.Z., Chase, S.C., Miner, E.D., Palluconi, F.D., 1976. Martian north pole summer temperatures—dirty water ice. Science 194, 1341–1344.

Kieffer, H.H., Titus, T.N., Mullins, K.F., Christensen, P.R., 2000. Mars south polar spring and summer behavior observed by TES: seasonal cap evolution controlled by frost grain size. J. Geophys. Res. 105, 9653–9700.

Langevin, Y., Poulet, F., Bibring, J.-P., Schmitt, B., Doute, S., Gondet, B., 2005. Summer evolution of the north polar cap of Mars as observed by OMEGA/Mars Express. Science 307, 1581–1584.

Leighton, R.R., Murray, B.C., 1966. Behavior of carbon dioxide and other volatiles on Mars. Science 153, 136–144.

Malin, M.C., Edgett, K.S., 2001. Mars Global Surveyor Mars Orbiter Camera: interplanetary cruise through primary mission. J. Geophys. Res. 106, 23429–23570.

Malin, M.C., Caplinger, M.A., Davis, S.D., 2001. Observational evidence for an active surface reservoir of solid carbon dioxide on Mars. Science 294, 2146–2148.

Mellon, M.T., 1996. Limits on the CO_2 content of the Martian polar deposits. Icarus 124, 268–279.

Murray, B.C., Soderblom, L.A., Cutts, J.A., Sharp, R.P., Milton, D.J., Leighton, R.B., 1972. Geological framework of the south polar region of Mars (A 4. 4). Icarus 17, 328.

Neumann, G.A., Abshire, J.B., Aharonson, O., Garvin, J.B., Sun, X., Zuber, M.T., 2003a. Mars Orbiter Laser Altimeter pulse width measurements and footprint-scale roughness. Geophys. Res. Lett. 30, 11.

Neumann, G.A., Smith, D.E., Zuber, M.T., 2003b. Two Mars years of clouds detected by the Mars Orbiter Laser Altimeter. J. Geophys. Res. 108, 1.

Nye, J.F., Durham, W.B., Schenk, P.M., Moore, J.M., 2000. The instability of a south polar cap on mars composed of carbon dioxide. Icarus 144, 449–455.

Paige, D.A., 1985. The annual heat balance of the Martian polar caps from Viking observations. Ph.D. Thesis, California Institute of Technology.

Prettyman, T.H., Feldman, W.C., Mellon, M.T., McKinney, G.W., Boynton, W.V., Karunatillake, S., Lawrence, D.J., Maurice, S., Metzger, A.E., Murphy, J.R., Squyres, S.W., Starr, R.D., Tokar, R.L., 2004. Composition and structure of the Martian surface at high southern latitudes from neutron spectroscopy. J. Geophys. Res. 109, 5001.

Seidelmann, P.K., et al., 2002. Report of the IAU/IAG Working Group on cartographic coordinates and rotational elements of the planets and satellites: 2000. Celestial Mech. Dyn. Astron. 82, 83–111.

Simpson, R.A., Tyler, G.L., 1981. Viking bistatic radar experiment— summary of first-order results emphasizing north polar data. Icarus 46, 361–389.

Smith, M.D., Pearl, J.C., Conrath, B.J., Christensen, P.R., 2000. Mars Global Surveyor Thermal Emission Spectrometer (TES) observations of dust opacity during aerobraking and science phasing. J. Geophys. Res. 105, 9539–9552.

Smith, D.E., et al., 2001a. Mars Orbiter Laser Altimeter: experiment summary after the first year of global mapping of Mars. Journal of Geophysical Research 106, 23689–23722.

Smith, D.E., Zuber, M.T., Neumann, G.A., 2001b. Seasonal variations of snow depth on Mars. Science 294, 2141–2146.

Smith, M.D., Conrath, B.J., Pearl, J.C., Christensen, P.R., 2002. Note: Thermal Emission Spectrometer Observations of Martian planet— encircling dust storm 2001A. Icarus 157, 259–263.

Stamnes, K., Tsay, S.-C., Jayaweera, K., Wiscombe, W., 1988. Numeri- cally stable algorithm for discrete-ordinate-method radiative transfer in multiple scattering and emitting layered media. Appl. Opt. 27, 2502–2509.

Sun, X., Neumann, G.A., Abshire, J.B., Zuber, M.T., 2006. Mars 1064-nm spectral radiance measurements using the receiver noise response of the Mars Orbiter Laser Altimeter. Appl. Opt. 45, 3960–3971.

Thomas, P.C., Squyres, S.W., Herkenhoff, K.E., Howard, A., Murray, B.C., 1992. Polar deposits of Mars. In: Kieffer, H.H., Jakosky, B.M., Snyder, C.W., Matthews, M.S. (Eds.), Mars. University of Arizona Press, pp. 767–795.

Thomas, P.C., Malin, M.C., Edgett, K.S., Carr, M.H., Hartmann, W.K., Ingersoll, A.P., James, P.B., Soderblom, L.A., Veverka, J., Sullivan, R., 2000. North–south geological differences between the residual polar caps on Mars. Nature 404, 161–164.

Thomas, P.C., Malin, M.C., James, P.B., Cantor, B.A., Williams, R.M.E., Gierasch, P., 2005. South polar residual cap of Mars: features, stratigraphy, and changes. Icarus 174, 535–559.

Titus, T.N., 2005. Mars polar cap edges tracked over 3 full Mars years. In: Proceedings of the 36th Annual Lunar and Planetary Science Conference 36, 1993.

Titus, T.N., Kieffer, H.H., Christensen, P.R., 2003. Exposed water ice discovered near the South Pole of Mars. Science 299, 1048–1051.

Tokar, R.L., Elphic, R.C., Feldman, W.C., Funsten, H.O., Moore, K.R., Prettyman, T.H., Wiens, R.C., 2003. Mars odyssey neutron sensing of the south residual polar cap. Geophys. Res. Lett. 30, 10–11.

Tomasko, M.G., Doose, L.R., Lemmon, M., Smith, P.H., Wegryn, E., 1999. Properties of dust in the Martian atmosphere from the Imager on Mars Pathfinder. J. Geophys. Res. 104, 8987–9008.

Wolff, M.J., Clancy, R.T., 2003. Constraints on the size of Martian aerosols from Thermal Emission Spectrometer observations. J. Geophys. Res. 108, 1.

Zuber, M.T., Smith, D.E., Solomon, S.C., Muhleman, D.O., Head, J.W., Garvin, J.B., Abshire, J.B., Bufton, J.L., 1992. The Mars observer laser altimeter investigation. J. Geophys. Res. 97, 7781–7797.

Zuber, M.T., et al., 1998. Observations of the north polar region of Mars from the Mars Orbiter Laser Altimeter. Science 282, 2053.